GDCh Research Article Angewandte International Edition Chemie www.angewandte.org

How to cite: *Angew. Chem. Int. Ed.* **2026**, *65*, e18738
doi.org/10.1002/anie.202518738

Organic Photovoltaics Hot Paper

Electrostatic and Geometric Regulation of "Third Terminal" in Non-Fullerene Acceptors for High-Performance Organic Photovoltaics

Shuhui Ding[+], Zheng Xu[+], Wenkai Zhao, Qiaorong Liu, Yu Zhang, Zhaoyang Yao, Yaxiao Guo, Guankui Long, Chenxi Li, Xiangjian Wan, and Yongsheng Chen**

Abstract: Inspired by the dominant role of 2-(3-oxo-2,3-dihydroinden-1-ylidene) malononitrile (INCN) terminal in regulating molecular packing, an innovative strategy to construct "third terminals" of non-fullerene acceptors (NFAs) is proposed by introducing INIC-mimicking motifs to molecular backbone center. Through delicate electrostatic and geometric regulation of INCN analogues (NQ, DCNQ, and TCNC), newly designed NFAs (CH56, CH57, and CH58) render not only an inverted distribution of molecular frontier orbitals, but also the substantial HOMO–LUMO overlap for CH56 while pronounced spatial separation for others. Especially, the puckered TCNC with the most LUMOs distribution yet minimal involvement in molecular packings drives CH58 to adopt a pseudo-three-dimensional (3D) packing network and inferior electron migration in sharp contrast to CH56. Moreover, the twisty CH57 and CH58 also exhibit unexpectedly quenched fluorescence due to the severe skeletal vibrations DCNQ and TCNC, further resulting in the large energy losses and poor photovoltaic performance. Finally, CH56-based OSCs yield a surprising open-circuit-voltage of 1.007 V for binary devices and an excellent 20.16% efficiency for ternary devices. Our trials on "third terminal" has enabled the extensive exploration of novel architectures of NFAs beyond conventional structural paradigms.

Introduction

Capitalizing on the remarkable advancements in non-fullerene acceptors (NFAs), particularly the ITIC- and Y-series derivatives,[1–5] organic solar cells (OSCs) have achieved a landmark milestone with surpassing 20% power conversion efficiencies (PCEs).[6–16] The synergistic integration of a planar central donor backbone with a strongly electron-withdrawing indandione terminal[2,17] establishes an innovative molecular paradigm, resolving the long-standing dilemma in OSCs of concurrently attaining the narrow bandgap, small voltage loss, high charge mobility, etc. Especially, the 2-(3-oxo-2,3-dihydroinden-1-ylidene) malononitrile (INCN) terminal[18,19] serves as a structural linchpin: 1) the carbonyl (-CO) and cyano (-CN) groups deliver dual electron-withdrawing effects (inductive and conjugative), which endow with INCN exceptionally strong electron-withdrawing capacity and thus the powerful modulation in energy level alignment of NFAs.[20,21] 2) The inherent coplanar conjugated π-system, including linear carbonyl/cyano groups and phenyl skeleton, facilitates efficient π–π stacking of NFAs and enhance their charge transport capabilities.[22–24] 3) The strong dipole–dipole interactions arising from the high polarity of -CO and -CN is also crucial for delivering compact/ordered packing of NFAs through sufficient secondary interactions.[25]

Notably, while both ITIC and Y6 exemplify classical INCN-terminated acceptors, Y-series NFAs consistently demonstrate superior charge carrier mobility.[26–30] This enhancement may stem from the fundamentally distinct aggregation behaviors.[31–34] Unlike the dominant end-to-end packing in most ITIC acceptors that mainly establishes one-dimensional (1D) charge-transport pathways,[35] Y-series acceptors usually possess additional modes involving with the central unit-to-central unit packings.[36] This distinctive packing architecture helps to form a three-dimensional (3D) intermolecular packing network which is expected to significantly optimize charge transfer/transport kinetics, for example, reducing exciton binding energies and charge recombination centers, etc.[37,38] It is also worth noting that such a 3D intermolecular packing network could be further

[*] S. Ding[+], Z. Xu[+], Q. Liu, Y. Zhang, Z. Yao, C. Li, X. Wan, Y. Chen
State Key Laboratory and Institute of Elemento-Organic Chemistry, The Centre of Nanoscale Science and Technology and Key Laboratory of Functional Polymer Materials, Renewable Energy Conversion and Storage Center (RECAST), Frontiers Science Center for New Organic Matter, College of Chemistry, Nankai University, Tianjin 300071, China
E-mail: zyao@nankai.edu.cn
yschen99@nankai.edu.cn

W. Zhao, G. Long
School of Materials Science and Engineering, National Institute for Advanced Materials, Renewable Energy Conversion and Storage Center (RECAST), Nankai University, Tianjin 300350, China

Y. Guo
State Key Laboratory of Separation Membranes and Membrane Processes, School of Chemistry, Tiangong University, Tianjin 300387, China

[+] Both authors contributed equally to this work.

Additional supporting information can be found online in the Supporting Information section

optimized through elaborately structural tailoring on central units of NFAs.[39,40] Especially, the two-dimensional (2D) conjugation extended central units usually bring about some unique dual molecular packing modes,[41,42] which is beneficial for obtaining more compact molecular packings and superior photovoltaic properties.[43,44]

Inspired by the pivotal role of INCN terminal and central units in regulating molecular packing, we proposed to introduce diverse electron-withdrawing INCN analogues into the center of molecular backbones, building them as "third terminals" of NFAs to enhance intermolecular packing strength. Through delicate electrostatic and geometric modulation of INCN analogues, three newly established NFAs of CH56, CH57, and CH58 were developed with [1,4]naphthoquinone (NQ), 11,11-dicyano-1,4-naphthoquinone methide (DCNQ) and 11,11,12,12-tetracyano-l,4-naphthochinodimethan (TCNC) as the "third terminal", respectively (Figure 1a). CH56, CH57, and CH58 exhibit not only an inverted distribution of molecular frontier orbitals but also distinct the highest occupied molecular orbital (HOMO) and the lowest unoccupied molecular orbital (LUMO) characteristics: CH56 demonstrates substantial orbital overlap, whereas CH57 and CH58 display pronounced spatial separation. Moreover, the puckered TCNC exhibits the most extensive LUMOs distribution yet minimal involvement in molecular packings as revealed by theoretical calculation and single crystal analysis. This structural characteristic drives CH58 to adopt a pseudo-3D packing network, further resulting in significantly inferior charge migration properties compared to that of CH56. Unexpectedly, both solutions and neat films of CH57 and CH58 exhibit nearly quenched fluorescence, which may be attributed to the severe skeletal vibrations of DCNQ and TCNC. This unfavorable luminescent property of CH57 and CH58 result in the larger energy loss and inferior device efficiency comparing to that of CH56. Finally, binary OSCs based on D18:CH56 achieve a surprising open circuit voltage of 1.007 V and a moderate PCE of 15.15%, much better than those of D18:CH57 and D18:CH58. When introducing CH6 acceptor,[44] an excellent PCE of 20.16% was further afforded by D18:CH6:CH56 ternary device.

Results and Discussions

The charge separation of photogenerated excitons represents the critical step in high performance organic photovoltaics, with its kinetics being fundamentally governed by the frontier molecular orbital distributions and energy level alignment.[45,46] Therefore, density functional theory (DFT) calculations were first conducted (Figure 1b), revealing a sufficient HOMO–LUMO overlap for CH56, but an obvious HOMO–LUMO separation for CH57 and CH58. Such a molecular frontier orbital distribution of CH57 and CH58 is quite desired by designing the new concept NFAs with thermal active delay fluorescent (TADF) features,[47] despite that no expectant phenomenon was observed in these near-infrared systems studied here. Additionally, the LUMOs of CH58 locate most on the TCNC unit rather than the conventional INIC terminal,[48–50] due to the strong electron-withdrawing capability of TCNC. With the gradually increased electron-withdrawing features from NQ to TCNC (as verified by the electrostatic potential maps in Figure S1), both the HOMO and LUMO energy levels downshifted greatly from CH56 to CH58. Moreover, the stepwise enlarged dipole moments could be also observed (0.09 Debye for CH56, 4.02 Debye for CH57 and 6.22 Debye for CH58), which may be helpful to form more compact molecular packings in some cases.[51–53] These results demonstrate the effectiveness in reconfiguring molecular frontier orbitals of NFAs through delicately tuning electrostatic potentials and geometries of "third terminals".

After several trials, single crystals suitable for X-ray diffraction were successfully obtained only for CH56 and CH58 and the new structures have been deposited in CCDC database with the number 2480678 for CH56 and 2480680 for CH58.[54] Meanwhile, the detailed parameters of single crystals were listed in Table S1. Given the most significant structural differences between CH56 and CH58, it may be sufficient to provide a guiding image to elucidate the impact of "third terminal" on molecular packings. As shown in Figure 2a, both CH56 and CH58 are featured with a banana-shape and helical geometry. Among them, CH56 shows a better planarity with an overall dihedral angle of ~11°, whereas CH58 exhibits a much larger dihedral angle of ~32°. Interestingly, NQ terminal on CH56 possesses a highly planar conformation, in sharp contrast to TCNC that adopts an exotic puckered backbone with four -CN groups out of plane. This twisty conformation of TCNC is mainly attributed to the bay-region steric congestion existing in anthraquinone analogues, which originates from the strong van der Waals repulsions between bulky -CN groups and adjacent bay-region hydrogens.[55] As illustrated in Figure 2b, CH58 forms a pseudo-3D intermolecular packing network bridged by very weak non-covalent interaction of -CN groups on TCNC rather than the conventional strong π–π stackings in CH56 (indicated by blue band).[56] This unique molecular packing topological structure of CH58 will have a negative impact on electron mobility, especially considering that the most probability distribution of LUMOs on TCNC but minimal participation in molecular packings.

The specific packing modes in crystals were presented in Figure 3. CH56 possessed the typical packing modes of "dual central-to-bridge" (dual C/b, $d_{\pi-\pi}$ = ~3.34 Å), "dual end-to-bridge" (dual E/b, $d_{\pi-\pi}$ = ~3.39 Å) and "end-to-end" (E/E, $d_{\pi-\pi}$ = ~3.43 Å). However, CH58 is featured with one unique "central-to-central" (C/C) interaction and two "dual end-to-bridge" packing modes (dual E/b-1, $d_{\pi-\pi}$ = ~3.50 Å and dual E/b-2, $d_{\pi-\pi}$ = ~3.27 Å). It is worth mentioning that the C/C mode in CH58 is composed by very weak non-covalent interactions rather than π–π stacking. The relatively large intermolecular potential of 137.8 kJ mol^{-1} for C/C mode may be mainly caused by the beneficial entanglement of alkyl chains.[57] The calculated electron/hole transfer integrals for each packing modes were summarized in Tables S2 and S3. The main packing modes in CH56 show the relatively large transfer integrals for both electron and hole. Particularly, the "E/E" mode possessed the largest electron

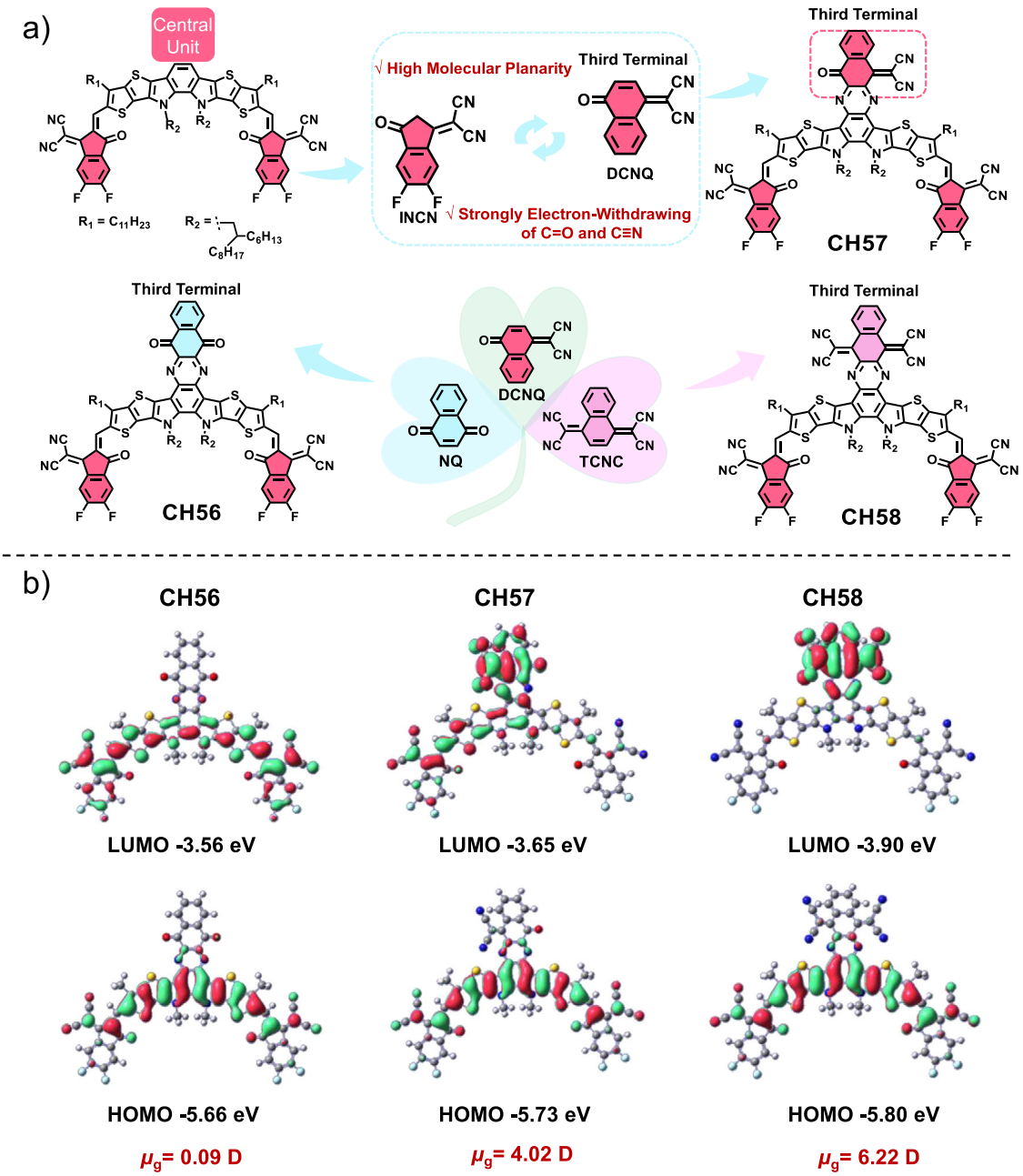

Figure 1. a) Design concept and chemical structures of CH56, CH57, and CH58. b) Spatial distributions of molecular frontier orbitals and dipole moments (μ_g) of CH56, CH57, and CH58. The HOMO and LUMO energy levels were also presented.

transfer integral of 42.93 meV, benefitting from both the compact packing of INIC terminals and their largest LUMO distribution probability. In sharp contrast, the LUMOs of CH58 mainly locate on TCNC unit, however, TCNC is almost completely absent from molecular stacking. This feature determines the electron transfer integrals approaching zero for all the three modes in CH58. On the other hand, the HOMOs of CH58 widely distribute on S,*N*-heteroacene and INIC terminal, making the "dual E/b-1" and "dual E/b-2" packing modes achieve the hole transfer integrals of 25.18 and 46.19 meV, respectively. This spatial inconsistency between LUMO distribution and molecular packing-involved segments results in no improvement (CH56) or even a significant decrease (CH58) in the electron transfer integral of NFAs, which should adversely affect the device performance greatly. Thus, a planar INIC-mimicking unit with the largest LUMO distribution and extensive participation in molecular packings is highly desired in the design of third terminal. As a consequence, CH56 neat film exhibits significantly higher electron mobility (8.09×10^{-4} cm^2 V^{-1} s^{-1}) yet lower hole mobility (0.72×10^{-4} cm^2 V^{-1} s^{-1}), whereas CH58 neat film demonstrates the opposite trend with inferior electron transport (2.07×10^{-4} cm^2 V^{-1} s^{-1}) but greatly improved hole mobility (5.94×10^{-4} cm^2 V^{-1} s^{-1}) in Figure S2 and Table S4.

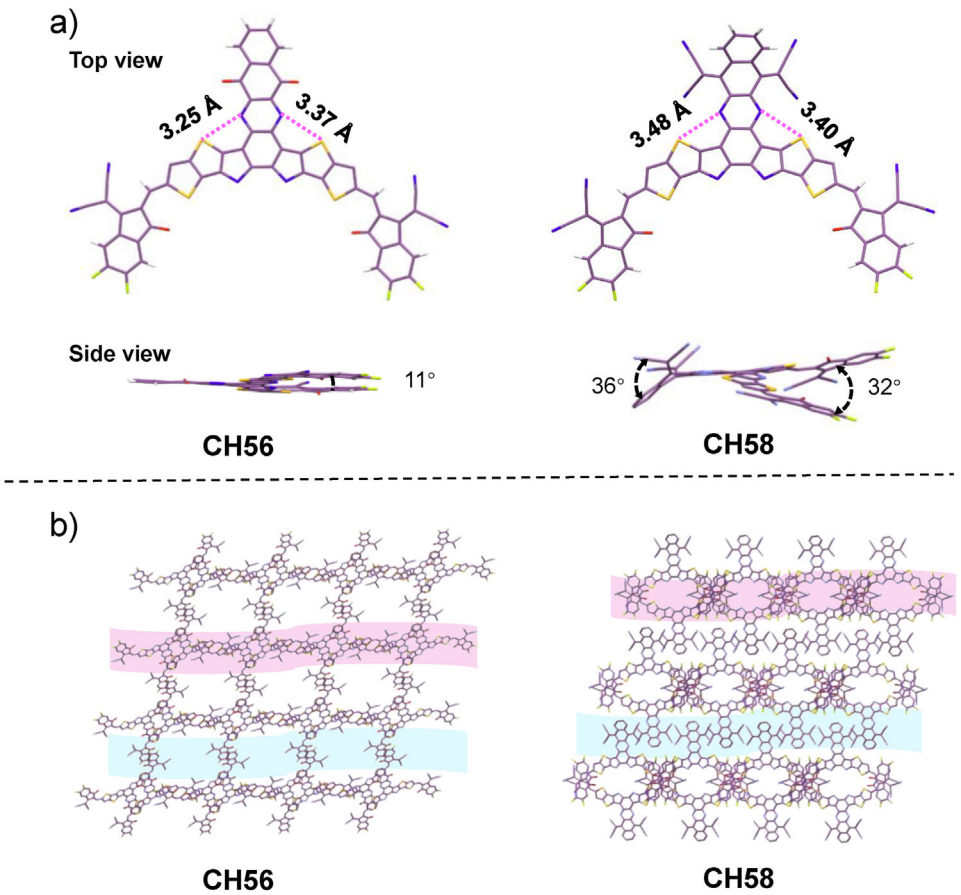

Figure 2. a) Monomolecular single crystallographic structure of CH56 and CH58 in top- and side-view. b) Molecular packing topological structures extracted from single crystals.

To sum up, the delicately tuning electrostatic and geometric characteristics of "third terminal" could govern the charge transport properties of NFAs through modulating molecular packing patterns and frontier orbital distribution in a targeted manner.

The synthetic routes of three NFAs were described in Schemes S1–S3. Meanwhile, the synthetic and characterization details were presented in Supporting Information. Figure 4a enumerated the energy levels of NFA films derived from cyclic voltammetry (CV) measurements (Figure S3) and the varying tendency correlates with the DFT prediction in Figure 1b. Three NFAs possess the nearly identical UV–visible (vis) absorption ranges in diluted solutions with the maximum absorption peak wavelengths of 712 nm for CH56, 711 nm for CH57 and 710 nm for CH58 (Figure 4b and Table S5). Interestingly, CH56 possesses the supreme molar extinction coefficient of 2.10×10^5 M^{-1} cm^{-1} compared to that of 1.86×10^5 M^{-1} cm^{-1} for CH57 and 1.70×10^5 M^{-1} cm^{-1} for CH58 (Figure S4). In addition, CH56 film affords an absorption coefficient of 1.09×10^5 cm^{-1}, larger than that of CH57 (1.03×10^5 cm^{-1}) and CH58 (0.97×10^5 cm^{-1}). The enhanced absorption of CH56 is benefitting from its more planar molecular geometry. Surprisingly, CH57 and CH58 exhibit unexpectedly quenched photoluminescence (PL) in both solutions and films, which is sharp contrast to that of CH56 (Figure 4c). To elucidate this anomalous phenomenon, we initially hypothesized that the non-emissive behavior might originate from the intrinsically twisty structures of DCNQ and TCNC. First, UV–vis absorption spectra of AQ, and TCAQ have been measured (Figure S6) and both of them exhibit the strong absorption. To our surprise, the analogue of TCAQ also exhibits the quite strong fluorescence emission (Figure 4d) comparing to that of AQ, thereby invalidating our initial hypothesis. The EQEs for electroluminescence (EQE_{EL}) reveals that CH57 and CH58 exhibit negligible external quantum efficiencies ($EQE_{EL} \approx 0\%$), indicating dominant non-radiative decay pathways (Figure 4e). Although no definitive conclusion has been reached, this anomalous fluorescence quenching may be attributed to one of the following factors: 1) severe skeletal vibrations. Temperature-dependent PL studies (Figure S7) under vacuum conditions reveal the emission enhancement at cryogenic temperatures, where molecular vibrations are substantially suppressed. 2) potential dark S_1 state.[58] The spatial separation of HOMO and LUMO orbitals may significantly enhance non-radiative decay rates through the effect of optically dark S_1 state, which is not conducive to fluorescence emission. Note that this unfavorable luminescent property of CH57 and CH58 could result in the larger energy loss and inferior device efficiency comparing to that of CH56.

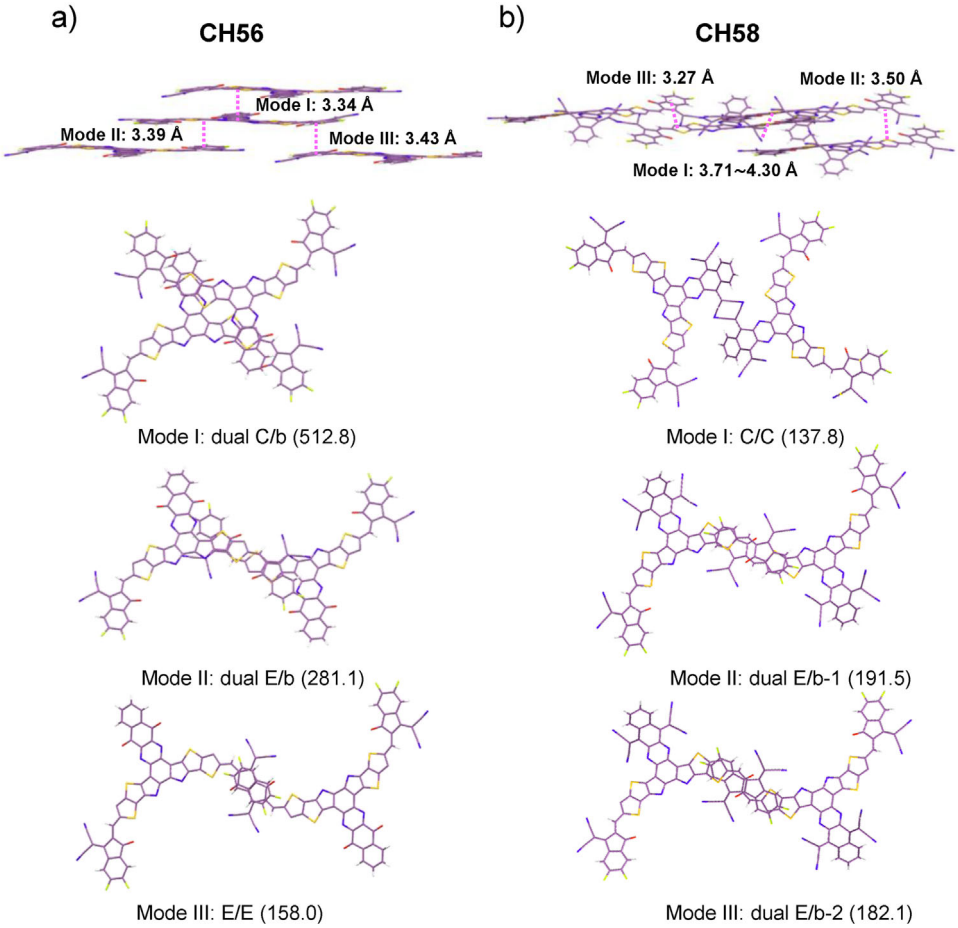

Figure 3. The detailed molecular packing analysis in single crystals of CH56 a) and CH58 b). Intermolecular packing modes and $\pi-\pi$ stacking distances ($d_{\pi-\pi}$) of interlayer including the main molecular packing modes with UNI intermolecular potentials >80 kJ mol^{-1}. The intermolecular potentials (kJ mol^{-1}) of each mode were included in brackets. C, b, and E represent central, bridge, and end units, respectively. The distances in Mode I of CH58 are obtained by measuring the distances between N atom on -CN group and adjacent N/C atoms on another molecules.

Notably, all the three NFAs have the relatively large dielectric constants of 4.33 for CH56, 3.78 for CH57 and 3.51 for CH58 (Figure S8), which is conducive to facilitating efficient exciton dissociation. To further investigate the packing behaviors of these three molecules in films, the 2D grazing incidence wide angle X-ray scattering (GIWAXS) of neat films were measured. As shown in Figure 4f and Figure S9; Table S6, all of CH56, CH57, and CH58 exhibit face-on molecular packing that facilitates vertical charge transport in films. Especially, CH56 possesses the smallest $d_{\pi-\pi}$ of 3.59 Å and largest crystal coherence length (CCL) of 17.08 Å in OOP direction compared to CH57 ($d_{\pi-\pi}$ of 3.68 Å; CCL of 14.32 Å) and CH58 ($d_{\pi-\pi}$ of 3.69 Å; CCL of 12.03 Å). The more compact and ordered packing of CH56 were determined by its more planar conformation and will facilitate charge transport theoretically.

D18 polymer[59] was selected as donor to study the "third terminal" effect on photovoltaic performance. The best *J*–*V* characteristics and external quantum efficiency (EQE) spectra were provided in Figure 5a,b and Table 1. Please find the device optimization details in Supporting Information (Table S7–S27; Figure S10 and S11). The binary OSCs based on D18:CH56 exhibited a surprising V_{OC} of 1.007 V, a short-circuit current density (J_{SC}) of 21.50 mA cm^{-2} and finally achieved a better PCE of 15.15% compared to that of D18:CH57-based OSCs with 13.39% PCE (V_{OC} = 0.901 V, J_{SC} = 19.25 mA cm^{-2}) and D18:CH58-based OSCs with 10.02% PCE (V_{OC} = 0.748 V, J_{SC} = 17.69 mA cm^{-2}). Moreover, the EQEs of CH56 is much higher than that of CH57 and CH58 (Figure 5b), agreeing well with the J_{SC} variation. In order to improve the performance of OSCs based on CH56, we further fabricated D18:CH6:CH56 ternary device, which reaches an excellent PCE of 20.16% with significantly enlarged J_{SC} of 27.65 mA cm^{-2} and fill factor (FF) of 81.08% (Table S27). Notably, the improvement of J_{SC} relies on enhancing the EQE absorption height (Figure 5b and Figure S11) and broadening the absorption edge (Figure 4b and Figure S12). To further unveil the reasons for better J_{SC} of CH56 than others on the premise of almost same light harvest (Figure S13), the charge dynamic studies on OSCs were conducted systematically. As displayed in Figure 5c, the plots between photocurrent density (J_{ph}) and effective voltage (V_{eff}) indicate that D18:CH56-based OSCs have the slightly better exciton dissociation efficiency (η_{diss}) of 97.7% than that

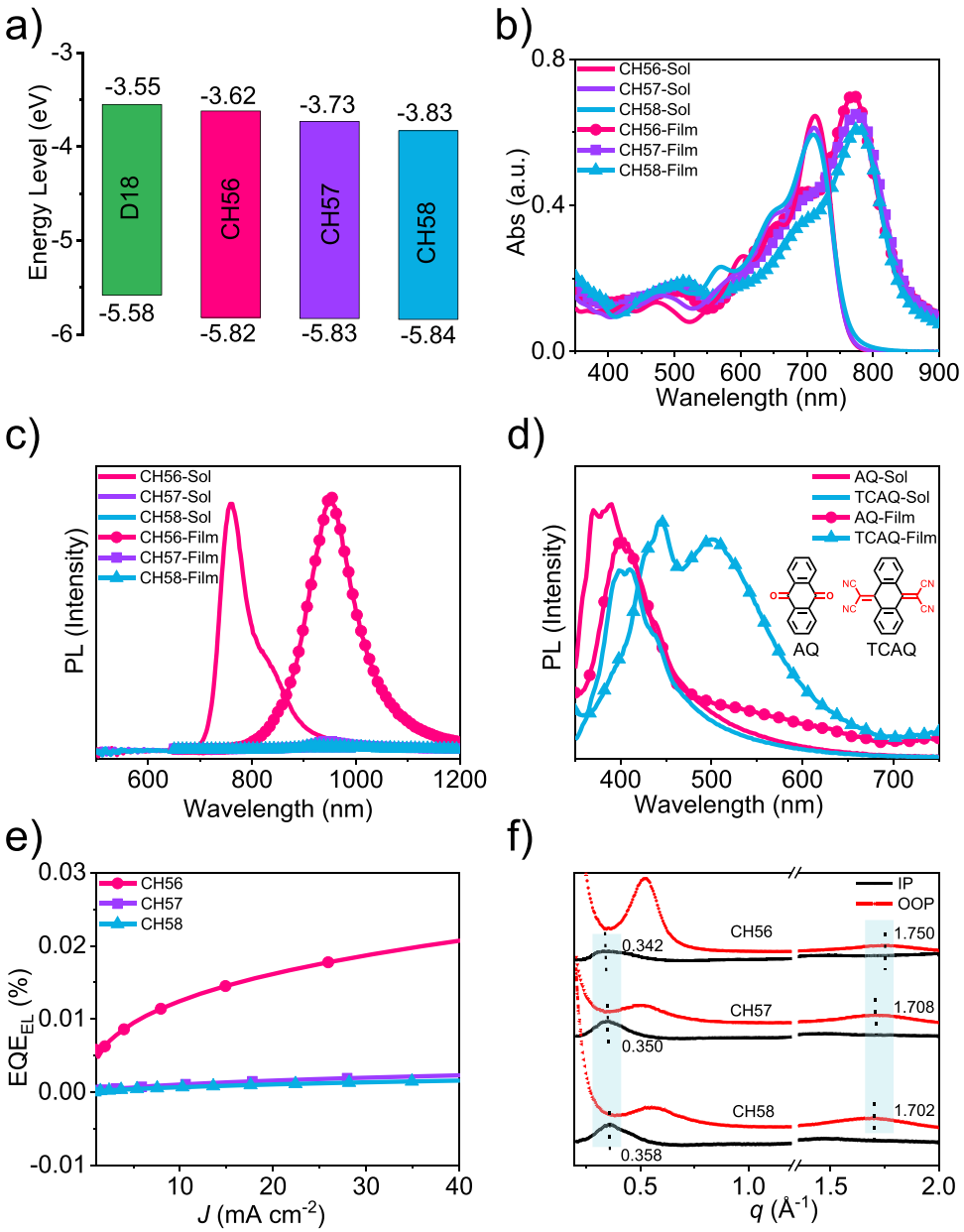

Figure 4. The physicochemical properties of CH56, CH57, and CH58. a) Energy levels derived from CV measurements. b) UV–visible (vis) spectra in both solutions and solid films. c,d) PL spectra of CH56, CH57, CH58, anthraquinone (AQ), and tetracyano-anthraquinodimethane (TCAQ) in both solutions and solid films. e) The spectra of electroluminescence EQEs of neat films. f) Line-cut profiles of 2D GIWAXS patterns in the in-plane (IP) and out-of-plane (OOP) directions.

Table 1: Summary of device parameters of the optimized OSCs.[a)]

Active layer	V_{OC} (V)	J_{SC} (mA cm^{-2})	$J_{SC}^{cal.}$ (mA cm^{-2})[b)]	FF (%)	PCE (%)
D18:CH56	1.007 (1.006 ± 0.002)	21.50 (20.97 ± 0.38)	20.56	70.01 (69.35 ± 0.72)	15.15 (14.62 ± 0.29)
D18:CH57	0.901 (0.902 ± 0.002)	19.25 (18.99 ± 0.36)	18.65	77.15 (76.37 ± 0.51)	13.39 (13.08 ± 0.26)
D18:CH58	0.748 (0.745 ± 0.004)	17.69 (17.91 ± 0.56)	17.05	75.78 (73.22 ± 2.51)	10.02 (9.76 ± 0.19)

[a)] Average parameters derived from 10 independent OSCs (Tables S11, S17, and S21). [b)] Current densities calculated from EQE plots.

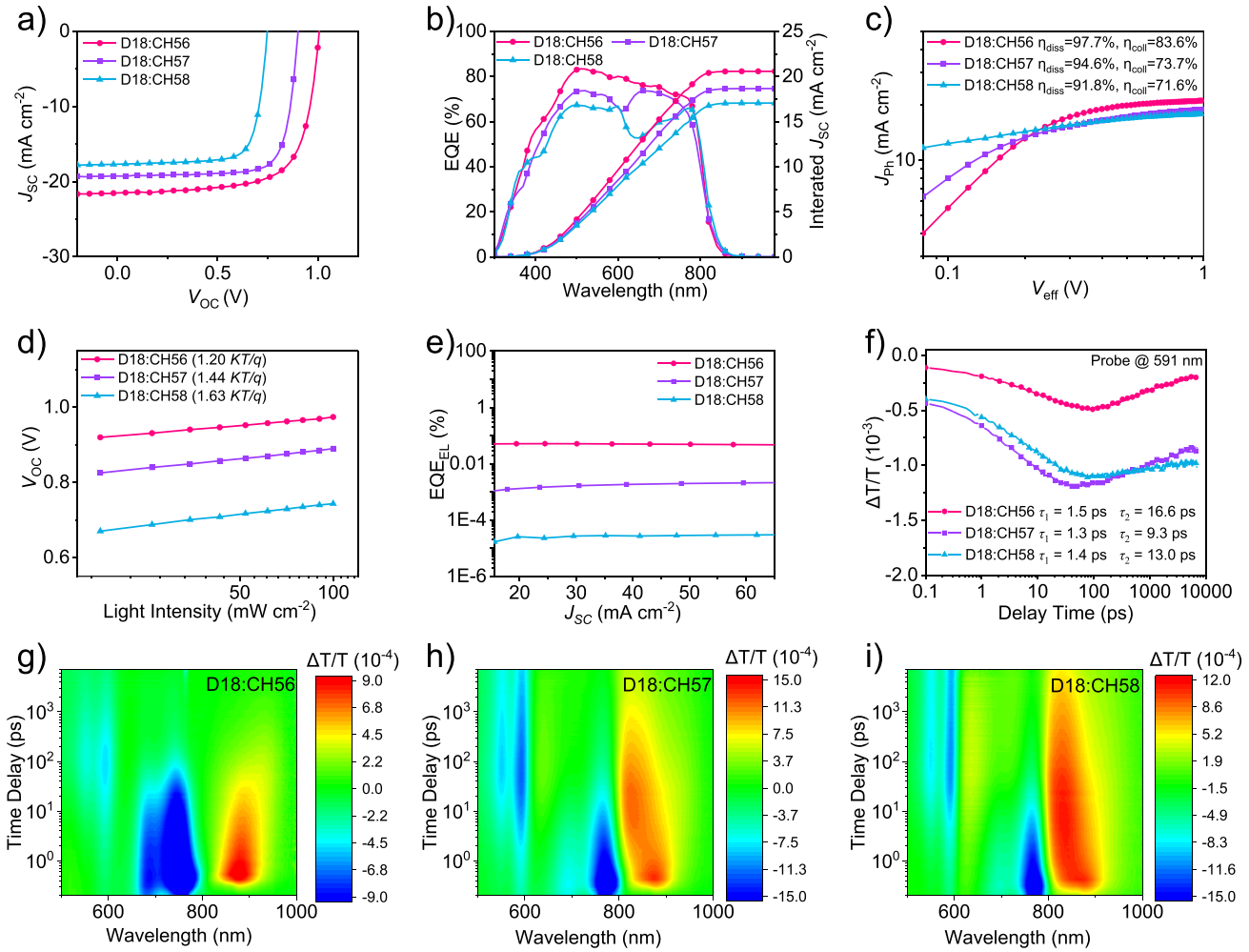

Figure 5. a) *J–V* curves. b) EQE plots and integrated J_{SC} curves. c) J_{ph} versus V_{eff} plots indicating η_{diss} and η_{coll}. d) P_{light} dependence of V_{OC}. e) Spectra of electroluminescence EQE. f) TA dynamics of GSB signals of D18 probed at 591 nm. g–i) 2D color plots of TA spectra under 700 nm excitation.

of 94.6% for D18:CH57 and 91.8% for D18:CH58, moreover, the greatly improved charge collection probability (η_{coll}) of 83.6% comparing to that of 73.7% for D18:CH57 and 71.6% for D18:CH58. As regards to the charge recombination, the dependences of J_{SC} and V_{OC} on light intensity (P_{light}) were recorded in Figure S14 and 5d, respectively. Despite the contrasting luminescent property of NFAs, the α values derived from the plots of J_{SC} versus P_{light} are approaching unity for three systems, implying the insignificant bimolecular recombination.[60] The plots of V_{OC} versus P_{light} render an S/(kT/q) value of 1.63 for D18:CH58, 1.44 for D18:CH57 and only 1.20 for D18:CH56, hinting the greatly suppressed trap-assisted charge recombination from CH58, CH57 to CH56.[61] Therefore, the charge recombination after exciton dissociation may play a dominant role in EQE/J_{SC} discrepancies. In similar fashion, the significantly decreased V_{OC} from CH56 to CH58 should be ascribed to not only the stepwise downshifted LUMO energy levels (Figure 4a) but also the increasing energy losses. The EQE_{EL} plots of D18:CH56, D18:CH57 and D18:CH58-based devices in Figure 5e render the quantitative non-radiative energy losses as 0.196, 0.292 and 0.396 eV, respectively[62] and the overall energy loss is consistent with this trend (Figure S15 and S16), which are in good accordance with the discussions above.

The exciton dynamics were further studied by using transient absorption (TA) spectroscopy under the photoexcitation of 700 nm. The TA dynamics of ground-state bleaching (GSB) signals of D18 probed at 591 nm were exhibited in Figure 5f and the 2D TA spectroscopy and coincident TA spectra at different delay times were shown in Figure 5g–i and Figure S17, respectively. In D/A blend films, the GSB signals of D18 imply the occurrence of hole transfer from NFAs to D18 donor, which could be also confirmed by the arising excited state absorption (ESA) peaks at approximate 876 nm (Figure S18).[63] By employing a biexponential function[64] the lifetimes of exciton dissociation/diffusion (τ_1/τ_2) were fitted to be 1.5/16.6, 1.3/9.3, and 1.4/13.0 ps for D18:CH56, D18:CH57 and D18:CH58, respectively (Figure 5f). D18:CH56 possesses the comparable exciton dissociation while slightly slower exciton diffusion comparing to the other two systems. Although the NAFs of CH57 and CH58 exhibit significantly quenched fluorescence, the exciton dissociation could also carry out

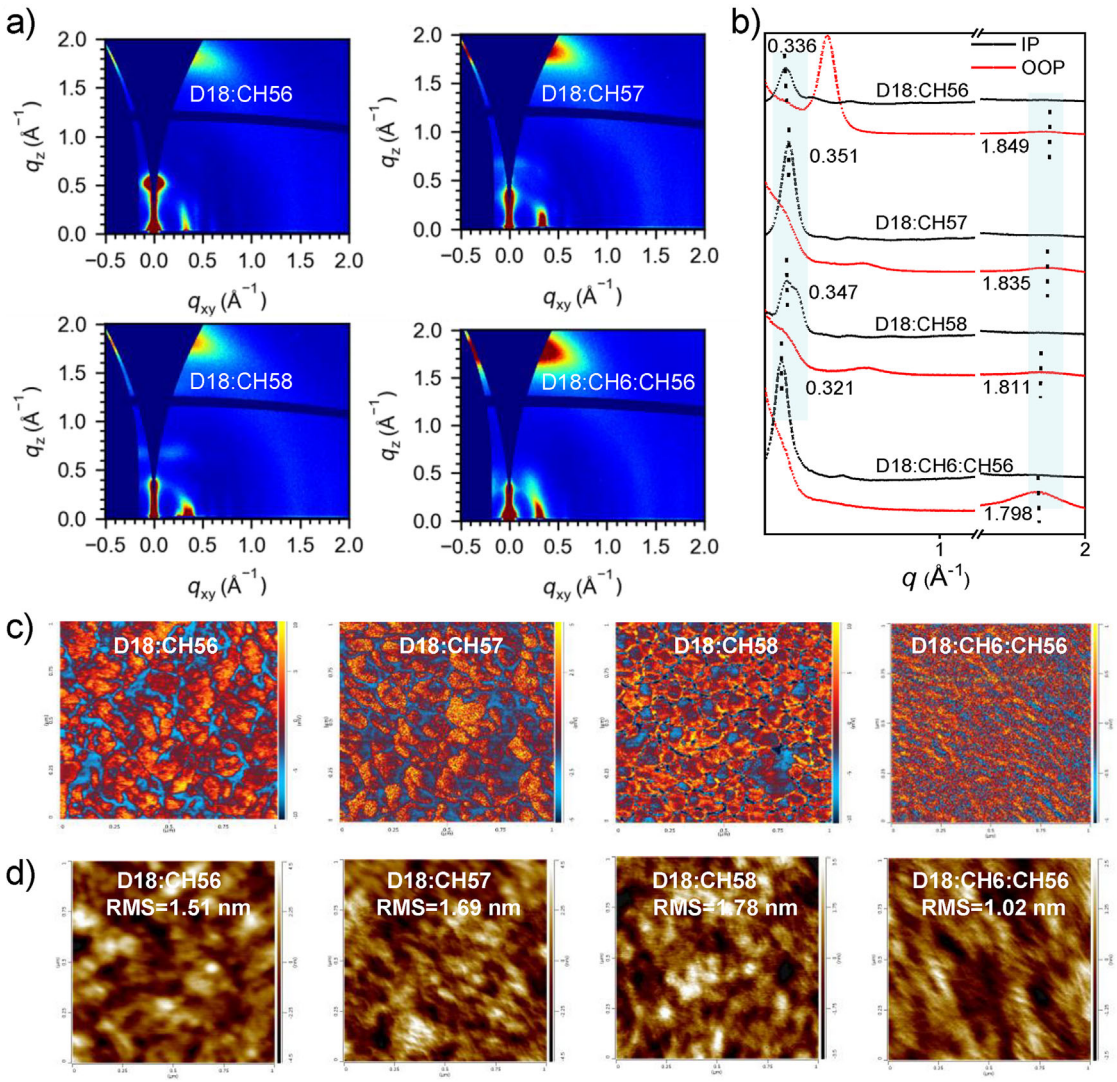

Figure 6. a) 2D GIWAXS patterns of blend films. b) Line-cut profiles of 2D GIWAXS patterns of blend films. c) AFM-IR images of blend films by detecting the IR signal of -CN at 2216 cm^{-1}. The acceptor and donor domains were marked in red and blue, respectively. d) AFM height images of blend films.

efficiently when blending with D18. This may be driven by the enlarged driving force for exciton dissociation from the perspective of molecular energy level arrangement (Figure 4a). It is worth noting that despite the comparable and even inferior charge generation dynamics, D18:CH56-based OSCs still achieved the best PCE owing to some other merits like the more suitable energy level arrangement, suppressed charge recombination and facilitated charge transport, etc. This demonstrates that the exciton dissociation process is not the pivotal factor of limiting PCEs of D18:CH57 and D18:CH58-based OSCs, as it could be also revealed by the characterization of device physics in Figure 5c,d. To further evaluate the charge transport property of blend films, hole mobility (μ_h) and electron mobility (μ_e) of active layers were measured (Figure S19 and Table S28). The device based on D18:CH56 affords the μ_h/μ_e of $11.20 \times 10^{-4}/2.42 \times 10^{-4}$ cm^{-2} V^{-1} s^{-1}, surpassing the $5.77 \times 10^{-4}/2.17 \times 10^{-4}$ cm^{-2} V^{-1} s^{-1} for D18:CH57 and $5.61 \times 10^{-4}/1.36 \times 10^{-4}$ cm^{-2} V^{-1} s^{-1} for D18:CH58 blend films. Meanwhile, D18:CH56 is featured with a faster charge extraction (0.29 μs) than D18:CH57 (0.35 μs) and D18:CH58 (0.54 μs) by transient photocurrent (TPC) decay analysis in Figure S20. By analyzing the data above, we could conclude that the inferior electron mobility and unbalanced μ_h/μ_e values greatly restricts the improvement of binary device efficiency.

We further studied the molecular packing behaviors in blend films by conducting GIWAXS measurements (Figure 6a,b and Table S29). Similar to that of neat films, all the blends exhibit the face-on packing orientation that facilitates charge transport. Among them, D18:CH56 possesses the smallest $d_{\pi-\pi}$ but largest CCL value in OOP direction comparing to D18:CH57 and D18:CH58. Generally, the compact and ordered packing is beneficial for improving charge migration in D18:CH56-based devices. It is interesting that the $d_{\pi-\pi}$ increased and CCL decreased after adding CH6 acceptor into D18:CH56 blend film. However, the markedly

improved μ_e and more balanced μ_h/μ_e could be still achieved by D18:CH6:CH56 blend comparing to D18:CH56 (Figure S21 and Table S28). This improvement may be determined by the optimized nanoscale morphology of active layers, thereby the atomic force microscopy-based infrared spectroscopy (AFM-IR) was further conducted (Figure S22). All the three D18:NFAs binary films show no fibrous morphology in Figure 6c, which may go against the efficient charge transport.[65] After adding CH6 into D18:CH56 blend, an obvious donor/acceptor interpenetrating fibrillar morphology can be observed. Particularly, the root-mean-square roughness (Rq) of film surface also decreased to 1.02 nm for D18:CH6:CH56 blend, from that of 1.51 nm for D18:CH56 (Figure 6d). The reduction of separation phase size for D18:CH6:CH56 blend should be caused by its improved donor/acceptor miscibility, which is indicated by the smaller Flory–Huggins interaction value (χ_{D-A}) of 0.014 comparing to that of 0.043 for D18:CH56, 0.203 for D18:CH57 and 0.373 for D18:CH58 blends (Figure S23 and Table S30).[66] Undoubtedly, the appropriate phase separation and fibrous film morphology contribute to the excellent charge transport in D18:CH6:CH56 blend, which plays a crucial role in reaching the best J_{SC} and FF of OSCs.

Conclusion

An innovative strategy to construct NFAs with exotic photoelectric features has been developed by introducing terminal-mimicking motifs to backbone center of NFAs. To be specific, we explored diverse electron-withdrawing INCN analogues (NQ, DCNQ and TCNC) and build them as the "third terminal" of NFAs. Through delicate electrostatic and geometric modulation of these INCN analogues, the newly established NFAs of CH56, CH57, and CH58 exhibit not only an inverted distribution of molecular frontier orbitals but also distinct HOMO–LUMO characteristics: CH56 demonstrates substantial orbital overlap, whereas CH57 and CH58 display pronounced spatial separation with unconventional LUMO distribution on DCNQ and TCNC rather than INIC terminal. An intensive study on single crystals reveals the puckered geometry of TCNC, which drives CH58 to adopt a pseudo-3D packing network. Owing to the most extensive LUMOs distribution yet minimal involvement in molecular packings for TCNC, the packing modes of CH58 demonstrates the negligible electron transfer integrals but quite large hole transfer integrals, which is in sharp contrast to that of CH56. Moreover, CH57 and CH58 exhibit unexpectedly quenched fluorescence and near to zero EQE_{EL}, potentially due to the severe skeletal vibrations of DCNQ/TCNC or optically dark excited state. Even so, the exciton dissociation could also carry out efficiently in D18:CH57 and D18:CH58 blend films under the adequate thermodynamic driving force. Unfortunately, the twisty geometry, unconventional molecular frontier orbital distribution and characteristic packing modes of CH58 synergistically result in the less compact/ordered molecular packings, markedly limited electron migration and larger non-radiative energy losses comparing to that of CH56. As a consequence, binary OSCs based on D18:CH56 achieve a surprising open circuit voltage of 1.007 V and a moderate PCE of 15.15%, much better than those of D18:CH57 and D18:CH58. When introducing CH56 as the third component into the D18:CH6 binary system, an excellent PCE of 20.16% was further afforded due to the significantly improved donor/acceptor interpenetrating fibrillar morphology. Our strategic construction of "third terminal" by exploring terminal-mimicking blocks on center backbones paves a new way to design high-performance NFAs beyond conventional structural paradigms.

Supporting Information

The Supporting Information is available free of charge, including materials synthesis, device characterization and stability measurements, charge mobility, CV, UV–vis spectra, NMR spectra (Figures S24–S38), mass spectra (Figures S39–S41) additional tables, etc.

Author Contributions

The synthetic works were carried out by Z.X. The device optimizations and measurements were carried out by S.D., and W.Z. performed the DFT calculations. Y.C. and Z.Y. conceived and directed the study, and also wrote the manuscript. Y.Z., Q.L., G.L., C.L., X.W., Y.G., and others helped to analyzed the data and commented on the manuscript.

Acknowledgements

The authors gratefully acknowledge the financial support from Ministry of Science and Technology of the People's Republic of China (National Key R&D Program of China, 2022YFB4200400), National Natural Science Foundation of China (22309090, 22479081, 52025033, 22361132530, and 52373189), Natural Science Foundation of Tianjin (23JCZDJC01160), and Haihe Laboratory of Sustainable Chemical Transformations.

Conflict of Interests

The authors declare no conflict of interest.

Data Availability Statement

The data that support the findings of this study are available from the corresponding author upon reasonable request.

Keywords: Energy loss · Non-fullerene acceptor · Orbital separation · Organic photovoltaic · Third terminal

[1] J. Yuan, Y. Zhang, L. Zhou, G. Zhang, H.-L. Yip, T.-K. Lau, X. Lu, C. Zhu, H. Peng, P. A. Johnson, M. Leclerc, Y. Cao, J. Ulanski, Y. Li, Y. Zou, *Joule* **2019**, *3*, 1140–1151, https://doi.org/10.1016/j.joule.2019.01.004.

[2] Y. Lin, J. Wang, Z.-G. Zhang, H. Bai, Y. Li, D. Zhu, X. Zhan, *Adv. Mater.* **2015**, *27*, 1170–1174, https://doi.org/10.1002/adma.201404317.

[3] S. Wang, S. Wang, J. Wang, N. Yu, J. Qiao, X. Xie, C. Li, M. S. Abbasi, R. Ding, X. Zhang, Y. Han, G. Lu, J. Zhang, X. Hao, Z. Tang, Y. Cai, H. Huang, *Adv. Ener. Mater.* **2025**, 2405205, https://doi.org/10.1002/aenm.202405205.

[4] Z. Chen, S. Zhang, J. Ren, T. Zhang, J. Dai, J. Wang, L. Ma, J. Qiao, X. Hao, J. Hou, *Adv. Mater.* **2024**, *36*, 2310390, https://doi.org/10.1002/adma.202310390.

[5] L. Zuo, X. Shi, S. B. Jo, Y. Liu, F. Lin, A. K.-Y. Jen, *Adv. Mater.* **2018**, *30*, 1706816, https://doi.org/10.1002/adma.201706816.

[6] H. Chen, Y. Huang, R. Zhang, H. Mou, J. Ding, J. Zhou, Z. Wang, H. Li, W. Chen, J. Zhu, Q. Cheng, H. Gu, X. Wu, T. Zhang, Y. Wang, H. Zhu, Z. Xie, F. Gao, Y. Li, Y. Li, *Nat. Mater.* **2025**, *24*, 444–453; https://doi.org/10.1038/s41563-024-02062-0.

[7] Y. Jiang, S. Sun, R. Xu, F. Liu, X. Miao, G. Ran, K. Liu, Y. Yi, W. Zhang, X. Zhu, *Nat. Ener.* **2024**, *9*, 975–986, https://doi.org/10.1038/s41560-024-01557-z.

[8] C. Li, J. Song, H. Lai, H. Zhang, R. Zhou, J. Xu, H. Huang, L. Liu, J. Gao, Y. Li, M. H. Jee, Z. Zheng, S. Liu, J. Yan, X.-K. Chen, Z. Tang, C. Zhang, H. Y. Woo, F. He, F. Gao, H. Yan, Y. Sun, *Nat. Mater.* **2025**, *24*, 433–443, https://doi.org/10.1038/s41563-024-02087-5.

[9] G. Yu, J. Gao, J. C. Hummelen, F. Wudl, A. J. Heeger, *Science* **1995**, *270*, 1789–1791, https://doi.org/10.1126/science.270.5243.1789.

[10] F. Lin, K. Jiang, W. Kaminsky, Z. Zhu, A. K. Y. Jen, *J. Am. Chem. Soc.* **2020**, *142*, 15246–15251, https://doi.org/10.1021/jacs.0c07083.

[11] Y. Ma, M. Zhang, S. Wan, P. Yin, P. Wang, D. Cai, F. Liu, Q. Zheng, *Joule* **2021**, *5*, 197–209, https://doi.org/10.1016/j.joule.2020.11.006.

[12] R. Englman, J. Jortner, *Mol. Phys.* **1970**, *18*, 145–164, https://doi.org/10.1080/00268977000100171.

[13] J. Benduhn, K. Tvingstedt, F. Piersimoni, S. Ullbrich, Y. Fan, M. Tropiano, K. A. McGarry, O. Zeika, M. K. Riede, C. J. Douglas, S. Barlow, S. R. Marder, D. Neher, D. Spoltore, K. Vandewal, *Nat. Ener.* **2017**, *2*, 17053

[14] M. Bixon, J. Jortner, J. Cortes, H. Heitele, M. E. Michel-Beyerle, *J. Phys. Chem.* **1994**, *98*, 7289–7299, https://doi.org/10.1021/j100081a010.

[15] Y. Dong, H. Cha, H. L. Bristow, J. Lee, A. Kumar, P. S. Tuladhar, I. McCulloch, A. A. Bakulin, J. R. Durrant, *J. Am. Chem. Soc.* **2021**, *143*, 7599–7603, https://doi.org/10.1021/jacs.1c00584.

[16] J. Miao, B. Meng, Z. Ding, J. Liu, L. Wang, *J. Mater. Chem. A* **2020**, *8*, 10983–10988, https://doi.org/10.1039/D0TA02865G.

[17] W. Tan, H. Gan, Y. Yu, F. He, Y. Ma, *Adv. Opt. Mater.* **2025**, *13*, 2402954, https://doi.org/10.1002/adom.202402954.

[18] G. He, Z. Li, X. Wan, J. Zhou, G. Long, S. Zhang, M. Zhang, Y. Chen, *J. Mater. Chem. A* **2013**, *1*, 1801–1809, https://doi.org/10.1039/C2TA00496H.

[19] H. Li, J. Li, C. Yang, J. Wang, D. H. Ryu, L. Ma, Y. Yang, W. S. Shin, S. Zhang, J. Hou, *Mater. Chem. C* **2023**, *11*, 6155–6161.

[20] L. Chen, C. Zhao, H. Yu, A. Sergeev, L. Zhu, K. Ding, Y. Fu, H. M. Ng, C. H. Kwok, X. Zou, J. Yi, X. Lu, K. S. Wong, H. Ade, G. Zhang, H. Yan, *Adv. Ener. Mater.* **2024**, *14*, 2400285, https://doi.org/10.1002/aenm.202400285.

[21] H. S. Kim, S. Rasool, W. S. Shin, C. E. Song, D.-H. Hwang, *ACS Appl. Mater. Interf.* **2020**, *12*, 50638–50647, https://doi.org/10.1021/acsami.0c13277.

[22] X. Ran, C. Zhang, D. Qiu, A. Tang, J. Li, T. Wang, J. Zhang, Z. Wei, K. Lu, *Adv. Mater.* **2025**, *37*, 2504805, https://doi.org/10.1002/adma.202504805.

[23] C. Lin, T. Kim, J. D. Schultz, R. M. Young, M. R. Wasielewski, *Nat. Chem.* **2022**, *14*, 786–793, https://doi.org/10.1038/s41557-022-00927-y.

[24] Y.-C. Wei, S. F. Wang, Y. Hu, L.-S. Liao, D.-G. Chen, K.-H. Chang, C.-W. Wang, S.-H. Liu, W.-H. Chan, J.-L. Liao, W.-Y. Hung, T.-H. Wang, P.-T. Chen, H.-F. Hsu, Y. Chi, P.-T. Chou, *Nat. Photonics* **2020**, *14*, 570–577, https://doi.org/10.1038/s41566-020-0653-6.

[25] H. Tian, K. Sun, D. Luo, Y. Wang, Z. Chen, L. Yu, G. Zhang, C. Yang, Z. Luo, *Sci. China Chem.* **2025**, https://doi.org/10.1007/s11426-025-2671-6.

[26] Y. Wang, W. Lan, N. Li, Z. Lan, Z. Li, J. Jia, F. Zhu, *Adv. Ener. Mater.* **2019**, *9*, 1900157, https://doi.org/10.1002/aenm.201900157.

[27] J. Luo, W. Zhou, Y. Li, C. Liao, X. Xu, Q. Peng, *Adv. Funct. Mater.* **2025**, *35*, 2501851, https://doi.org/10.1002/adfm.202501851.

[28] X. Liao, Q. Xie, Y. Guo, Q. He, Z. Chen, N. Yu, P. Zhu, Y. Cui, Z. Ma, X. Xu, H. Zhu, Y. Chen, *Ener. Environ. Sci.* **2022**, *15*, 384–394, https://doi.org/10.1039/D1EE02858H.

[29] S. Liang, S. Li, Y. Zhang, T. Li, H. Zhou, F. Jin, C. Sheng, G. Ni, J. Yuan, W. Ma, H. Zhao, *Adv. Funct. Mater.* **2021**, *31*, 2102764, https://doi.org/10.1002/adfm.202102764.

[30] Q. An, F. Zhang, W. Gao, Q. Sun, M. Zhang, C. Yang, J. Zhang, *Nano Ener.* **2018**, *45*, 177–183, https://doi.org/10.1016/j.nanoen.2017.12.050.

[31] X. Ding, Y. F. Ding, C. Huang, Y. Li, M. Zhang, C. Zhu, Z. Li, *Small* **2024**, *20*, 2311715, https://doi.org/10.1002/smll.202311715.

[32] Y. Shi, L. Zhu, Y. Yan, M. Xie, G. Liang, J. Qiao, J. Zhang, X. Hao, K. Lu, Z. Wei, *Adv. Ener. Mater.* **2023**, *13*, 2300458, https://doi.org/10.1002/aenm.202300458.

[33] K. Yuan, C. Wang, L. Ma, Z. Chen, J. Ren, W. Wang, H. Li, J. Zhu, J. Hou, S. Zhang, *J. Mater. Chem. A* **2025**, *13*, 12673–12680

[34] W. Zhu, A. P. Spencer, S. Mukherjee, J. M. Alzola, V. K. Sangwan, S. H. Amsterdam, S. M. Swick, L. O. Jones, M. C. Heiber, A. A. Herzing, G. Li, C. L. Stern, D. M. DeLongchamp, K. L. Kohlstedt, M. C. Hersam, G. C. Schatz, M. R. Wasielewski, L. X. Chen, A. Facchetti, T. J. Marks, *J. Am. Chem. Soc.* **2020**, *142*, 14532–14547, https://doi.org/10.1021/jacs.0c05560.

[35] J. Tan, Y. Zhao, G. Li, S. Yang, C. Huang, H. Yu, *Adv. Funct. Mater.* **2022**, *32*, 2209094, https://doi.org/10.1002/adfm.202209094.

[36] Y. Cui, P. Zhu, X. Shi, X. Liao, Y. Chen, *Phys. Chem. C* **2021**, *125*, 10250–10259.

[37] C. Liu, N. Qiu, H. Liu, Y. Kan, Y. Sun, K. Gao, C. Li, Y. Lu, *Adv. Funct. Mater.* **2025**, *35*, 2414292, https://doi.org/10.1002/adfm.202414292.

[38] M. Liu, X. Ge, X. Jiang, F. Guo, S. Gao, Q. Peng, L. Zhao, Y. Zhang, *Adv. Funct. Mater.* **2023**, *33*, 2300214, https://doi.org/10.1002/adfm.202300214.

[39] H. Chen, T. Zhao, L. Li, P. Tan, H. Lai, Y. Zhu, X. Lai, L. Han, N. Zheng, L. Guo, F. He, *Adv. Mater.* **2021**, *33*, 2102778, https://doi.org/10.1002/adma.202102778.

[40] W. Gao, R. Ma, L. Zhu, L. Li, F. R. Lin, T. A. Dela Peña, J. Wu, M. Li, W. Zhong, X. Wu, Z. Fink, C. Tian, F. Liu, Z. Wei, A. K. Y. Jen, G. Li, *Adv. Ener. Mater.* **2024**, *14*, 2304477, https://doi.org/10.1002/aenm.202304477.

[41] Z. Yao, X. Wan, C. Li, Y. Chen, *Acc. Mater. Res.* **2023**, *4*, 772–785, https://doi.org/10.1021/accountsmr.3c00093.

[42] Z. Luo, W. Wei, R. Ma, G. Ran, M. H. Jee, Z. Chen, Y. Li, W. Zhang, H. Y. Woo, C. Yang, *Adv. Mater.* **2024**, *36*, 2407517, https://doi.org/10.1002/adma.202407517.

[43] P. Li, X. Meng, K. Jin, Z. Xu, J. Zhang, L. Zhang, C. Niu, F. Tan, C. Yi, Z. Xiao, Y. Feng, G. W. Wang, L. Ding, *Carbon Ener.* **2022**, *5*, e250.

[44] H. Chen, H. Liang, Z. Guo, Y. Zhu, Z. Zhang, Z. Li, X. Cao, H. Wang, W. Feng, Y. Zou, L. Meng, X. Xu, B. Kan, C. Li, Z. Yao, X. Wan, Z. Ma, Y. Chen, *Angew. Chem. Int. Ed.* **2022**, *61*, e202209580, https://doi.org/10.1002/anie.202209580.
[45] C. Liu, Y. Lian, J. Song, J. Liu, Z. Bi, W. Ma, Y. Sun, *Adv. Funct. Mater.* **2025**, *35*, 2417786
[46] S. Li, C.-Z. Li, M. Shi, H. Chen, *ACS Ener. Lett.* **2020**, *5*, 1554–1567, https://doi.org/10.1021/acsenergylett.0c00537.
[47] T. Hatakeyama, K. Shiren, K. Nakajima, S. Nomura, S. Nakatsuka, K. Kinoshita, J. Ni, Y. Ono, T. Ikuta, *Adv. Mater.* **2016**, *28*, 2777–2781, https://doi.org/10.1002/adma.201505491.
[48] R. Zeng, J. Deng, X. Xue, S. Tan, L. Kan, Y. Lin, W. Zhong, L. Zhu, F. Han, Y. Zhou, X. Gao, M. Zhang, Y. Zhang, S. Xu, F. Liu, *Angew. Chem. Int. Ed.* **2025**, *64*, e202420453.
[49] K. Tu, Y. Chen, T. Duan, S. Duan, D. Hu, L. Liu, G. Tian, T. Gu, H. Liu, X. Lu, C. Uragami, H. Hashimoto, P. Huang, Z. Xiao, *Adv. Funct. Mater.* **2025**, e11914, https://doi.org/10.1002/adfm.202511914.
[50] H. Liu, Y. Geng, Z. Xiao, L. Ding, J. Du, A. Tang, E. Zhou, *Adv. Mater.* **2024**, *36*, 2404660, https://doi.org/10.1002/adma.202404660.
[51] T. Xu, Z. Luo, R. Ma, Z. Chen, T. A. Dela Peña, H. Liu, Q. Wei, M. Li, C. e. Zhang, J. Wu, X. Lu, G. Li, C. Yang, *Angew. Chem. Int. Ed.* **2023**, *62*, e202304127
[52] D. L. Ma, Q. Q. Zhang, C. Z. Li, *Angew. Chem. Int. Ed.* **2023**, *62*, e202214931, https://doi.org/10.1002/anie.202214931.
[53] T. Duan, Q. Chen, D. Hu, J. Lv, D. Yu, G. Li, S. Lu, *Trends Chem.* **2022**, *4*, 773–791, https://doi.org/10.1016/j.trechm.2022.06.007.
[54] Deposition Numbers 2480678 (for CH56) and 2480680 (for CH58) contain the supplementary crystallographicdata for this paper. These data are provided free of charge by the joint Cambridge Crystallographic Data Centre and Fachinformationszentrum Karlsruhe Ac.
[55] S. Xu, Q. He, X. Xue, J. Deng, F. Han, F. Xie, X. Jiao, L. Zhou, R. Zeng, Z. Wang, M. Zhang, L. Zhu, H. Jing, Y. Zhang, F. Liu, *Angew. Chem. Int. Ed.* **2025**, *64*, e202507616, https://doi.org/10.1002/anie.202507616.
[56] X. Liao, M. Liu, W. Xie, J. Wang, P. Zhu, S. Yu, Y. Fu, X. Lu, K. Feng, X. Guo, Y. Chen, *Adv. Funct. Mater.* **2024**, *34*, 2405728, https://doi.org/10.1002/adfm.202405728.
[57] Y. Li, X. Jia, X. Bi, K. Wang, W. Zhao, X. Cao, Z. Yao, Y. Guo, Z. Zhang, G. Long, C. Li, X. Wan, Y. Chen, *J. Mater. Chem. A* **2025**, *13*, 12339–12348.
[58] G. Song, T. He, R. Wang, Y. Ouyang, N. Jain, S. Liu, B. Kan, Y. Shang, J. Li, X. Wang, Z. Yao, X. Wan, C. Li, W. Ma, Y. Zhao, G. Long, C. Zhang, F. Gao, Y. Chen, *Angew. Chem. Int. Ed.* **2025**, *64*, e202506357, https://doi.org/10.1002/anie.202506357.
[59] Q. Liu, Y. Jiang, K. Jin, J. Qin, J. Xu, W. Li, J. Xiong, J. Liu, Z. Xiao, K. Sun, S. Yang, X. Zhang, L. Ding, *Sci. Bull.* **2020**, *65*, 272–275.
[60] A. K. K. Kyaw, D. H. Wang, V. Gupta, W. L. Leong, L. Ke, G. C. Bazan, A. J. Heeger, *ACS Nano* **2013**, *7*, 4569–4577, https://doi.org/10.1021/nn401267s.
[61] C. M. Proctor, M. Kuik, T.-Q. Nguyen, *Prog. Polym. Sci.* **2013**, *38*, 1941–1960, https://doi.org/10.1016/j.progpolymsci.2013.08.008.
[62] Y. Chen, X. Duan, J. Zhang, Z. Ge, H. Ma, X. Sun, H. Zhang, J. Gao, X. Wang, X. Wang, Z. Tang, R. Yang, F. Gao, Y. Sun, *Ener. Environ. Sci.* **2025**, *18*, 6214–6223, https://doi.org/10.1039/D5EE01525A.
[63] R. Wang, C. Zhang, Q. Li, Z. Zhang, X. Wang, M. Xiao, *J. Am. Chem. Soc.* **2020**, *142*, 12751–12759, https://doi.org/10.1021/jacs.0c04890.
[64] A. J. Gillett, A. Privitera, R. Dilmurat, A. Karki, D. Qian, A. Pershin, G. Londi, W. K. Myers, J. Lee, J. Yuan, S.-J. Ko, M. K. Riede, F. Gao, G. C. Bazan, A. Rao, N. Thuc-Quyen, D. Beljonne, R. H. Friend, *Nature* **2021**, *597*, 666–671, https://doi.org/10.1038/s41586-021-03840-5.
[65] L. Zhu, M. Zhang, J. Xu, C. Li, J. Yan, G. Zhou, W. Zhong, T. Hao, J. Song, X. Xue, Z. Zhou, R. Zeng, H. Zhu, C.-C. Chen, R. C. I. MacKenzie, Y. Zou, J. Nelson, Y. Zhang, Y. Sun, F. Liu, *Nat. Mater.* **2022**, *21*, 656–663, https://doi.org/10.1038/s41563-022-01244-y.
[66] S. Nilsson, A. Bernasik, A. Budkowski, E. Moons, *Macromolecules* **2007**, *40*, 8291–8301, https://doi.org/10.1021/ma070712a.

Manuscript received: August 26, 2025
Revised manuscript received: October 29, 2025
Manuscript accepted: October 29, 2025
Version of record online: November 07, 2025